Unsupervised radiometric change detection from synthetic aperture radar images

Thomas Bultingaire, Inès Meraoumia, Christophe Kervazo, Loïc Denis, Florence Tupin

Unsupervised radiometric change detection from synthetic aperture radar images

Thomas Bultingaire*, Inès Meraoumia*, Christophe Kervazo*, Loïc Denis†,*, and Florence Tupin*
* LTCI, Télécom Paris, Institut Polytechnique de Paris, 91120 Palaiseau, France
† Université Jean Monnet Saint-Etienne, CNRS, Institut d'Optique Graduate School, Laboratoire Hubert Curien UMR 5516, F-42023, Saint-Étienne, France

***Abstract*—Change detection is an important data processing task in remote sensing, with applications such as deforestation monitoring or natural disaster assessment. Synthetic Aperture Radar (SAR) imaging offers key advantages for change detection, in particular due to its robustness to weather condition and cloud coverage. Because of the speckle phenomenon, the intensity of SAR images suffer from strong fluctuations, making the detection of radiometric changes challenging. Our method builds on a recently introduced self-supervised despeckling technique. It estimates despeckling uncertainty to better identify meaningful differences between two despeckled images. Conformal prediction permits to approach the change detection problem from the angle of anomaly detection. Thus, we develop a fully unsupervised change detection approach with a controlled probability of false alarm. Experimental results on TerraSAR-X satellite images with metric resolution show the capability of our method to detect changes without any supervision.**

***Index Terms*—unsupervised change detection, SLC SAR, CFAR, conformal prediction, despeckling uncertainty**

I. Introduction

Synthetic Aperture Radar (SAR) is an active remote sensing imaging modality based on the emission of short pulses of radio waves and the measurement of the echoes back-scattered by the surface of the Earth. After synthesis, a focused SAR image in Single Look Complex (SLC) format corresponds to an array of complex values. In contrast to optical imaging, SAR images are not affected by clouds or by daily and seasonal variations of the sun light and of the corresponding shadows. Radar imaging is therefore well-adapted to perform change detection. Yet, SAR images suffer from strong fluctuations due to the speckle phenomenon that arises from the constructive and destructive interferences between multiple echoes collected by the radar antenna for a given resolution cell. It is challenging to distinguish an intensity variation due to a radiometric change of the SAR scene from a fluctuation due solely to the speckle phenomenon. Adequate processing is necessary to limit erroneous change detections.

The task of change detection in Earth observation corresponds to the localization of changes that occur on the ground between two or more dates. Such a monitoring has a very large domain of applications, including deforestation and sea ice monitoring, or disaster assessment such as landslide mapping and assessment of damages created by floods, forest fires, or earthquakes [1].

Several recent change detection methods for SAR, optical/multi-spectral or multimodal [2] imaging are based on supervised deep-learning [3]–[6] which requires manually labeled images, a very time-consuming step. Some methods, like [7], use a pretext task in order to pre-train a feature extractor in order to reduce the amount of required labeled data or to improve performance. These methods can achieve semantic change detection and, thanks to the ground truths, can be adapted to a specific type of change, which is extremely dependent on the application.

Unsupervised methods can be split in two main categories. First, an unsupervised classification method can be applied to the output of a feature extractor, pre-trained via a pretext task [8] or contrastive-learning [9]. The unsupervised classifier can be based on k-means clustering [10], Change Vector Analysis [11], Markov Random Field [11], [12], or an automatic thresholding algorithm [13]. Second, several methods use multiple steps: they perform an unsupervised clustering, for example with the fuzzy c-means [12], to classify pixels into three classes, i.e., changed, unchanged and undetermined. Then, changed and unchanged pixels are used as pseudo-labels for the supervised training of a change detection model generally composed of a feature extractor followed by fully-connected layers for classification. This kind of unsupervised approach has been employed with various feature-extractor architectures such as Convolutional Neural Networks (CNN) and attention mechanisms [14], Transformers [15], with a specific management of multiscale features [16] or by mixing spatial and frequency features [17]. Some also use a clustering algorithm during the loss evaluation [18], or rely on an iterative process like [19] which aims to refine progressively the labels. The same is possible for manual labels that are considered unreliable [20].

None of these methods is designed to produce Constant False Alarm Rate (CFAR) change detection maps, i.e. the same probability of false alarm everywhere. In contrast, [21] takes high-resolution multivariate SAR heterogeneity into account with a robust spherically invariant random vectors model, and derives statistics from generalized likelihood ratio test to verify theoretically CFAR property. We also design a change detection approach with the goal of obtaining a CFAR

The work was partially supported by Agence de l'Innovation de Défense – AID - via Centre Interdisciplinaire d'Etudes pour la Défense et la Sécurité – CIEDS - (project 2023 - ALIA).

property. Our contributions are the following:

- we design an unsupervised change detection method for SAR images that is robust to speckle fluctuations,
- we propose a self-supervised learning strategy to estimate the uncertainty of any despeckling method that can be applied to half-look SAR images[1]
- we address the change detection task as an anomaly detection and use the decomposition of SAR images into real and imaginary parts as two views of the same scene without change, to calibrate our change detection method and control the probability of false alarm.

II. Methodology

Our objective is to construct a change detection algorithm with a CFAR property. We consider the observation of a scene at two different acquisition dates t_i and t_j, corresponding to two N-pixels SAR images $\boldsymbol{z}_i \in \mathbb{C}^N$ and $\boldsymbol{z}_j \in \mathbb{C}^N$ after proper co-registration.

To identify reflectivity changes between these two images, one could compute the differences between the intensities $|\boldsymbol{z}_i|^2$ and $|\boldsymbol{z}_j|^2$ (where the squared modulus is applied pixelwise). Because of speckle fluctuations, this would lead to extremely noisy change detection maps with errors located mainly in the bright areas of the images where the variance of speckle is the largest (see Fig. 1b). The variance of speckle can be stabilized by a log-transform, it is therefore more relevant to compare log-intensities rather than the intensities, but due to speckle fluctuations, these images are still too noisy (Fig. 1c). Better yet is the comparison of despeckled images, i.e., the estimated log-reflectivity images $\log \widehat{\boldsymbol{r}}_i \in \mathbb{R}^N$ and $\log \widehat{\boldsymbol{r}}_j \in \mathbb{R}^N$ obtained with a despeckling algorithm (Fig. 1d). However, denoising methods notoriously perform better in large stationary areas and more poorly close to edges or point-like structures and in textured areas with a small spatial extent. The variance of estimators of the SAR reflectivity is thus non-stationary. Failing to account for the uncertainties of the despeckling method leads to a concentration of false alarms detection in the areas that are difficult to denoise, and thus a non-CFAR change detector.

To obtain a change detection technique that is both robust to speckle fluctuations and with a CFAR behavior, we propose to apply despeckling and uncertainty quantification. In section II-A, we show how to estimate despeckling uncertainty in a self-supervised manner for methods that can be applied to half-look SAR images. Then, in section II-B, we use conformal prediction [22] to calibrate our change detection method, inspired by anomaly detection techniques [23].

A. Self-supervised uncertainty quantification

The paper [24] introduced a self-supervised despeckling strategy based on the decomposition of a SAR image $\boldsymbol{z} \in \mathbb{C}^N$ into its real and imaginary components $\boldsymbol{a} \in \mathbb{R}^N$ and $\boldsymbol{b} \in \mathbb{R}^N$. Under Goodman's fully developed speckle model, the phase of a SAR image is uniformly distributed and $\boldsymbol{a}$ and $\boldsymbol{b}$ are independent and identically distributed. The images $\boldsymbol{a}^2$ and $\boldsymbol{b}^2$ can be used like two independent observations of the same scene, in the absence of change, with twice the amount of speckle compared to the full intensity image $|\boldsymbol{z}|^2 = \boldsymbol{a}^2 + \boldsymbol{b}^2$. In [24], this remark led to the training of a despeckling framework using the Noise2Noise principle [25], only $2\boldsymbol{a}^2$ was fed to the network and the neg-log-likelihood $-\log \mathrm{p}(2\boldsymbol{b}^2|\widehat{\boldsymbol{r}}(\boldsymbol{a}))$ was used to learn to predict the reflectivity common to the two components $\boldsymbol{a}$ and $\boldsymbol{b}$. In this paper, we leverage the decomposition into real and imaginary parts to characterize the uncertainties of despeckling methods. Indeed, the reflectivities $\widehat{\boldsymbol{r}}(\boldsymbol{a})$ and $\widehat{\boldsymbol{r}}(\boldsymbol{b})$ of a given SAR image are expected to differ more strongly in areas of high uncertainty. The direct computation of the absolute differences $\boldsymbol{\delta}_{\boldsymbol{a}}^{\boldsymbol{b}} = |\log \widehat{\boldsymbol{r}}(\boldsymbol{a}) - \log \widehat{\boldsymbol{r}}(\boldsymbol{b})|$, however, is not a reliable estimate due to the variance of the reflectivity estimator. We are rather interested in the expectation $\mathbb{E}\big[\boldsymbol{\delta}_{\boldsymbol{a}}^{\boldsymbol{b}}\big]$. This can be learned using the Noise2Noise principle [25] by the network $g_{\boldsymbol{\theta}} : (\boldsymbol{a}, \widehat{\boldsymbol{r}}(\boldsymbol{a})) \mapsto \widehat{\boldsymbol{\mu}}_{\boldsymbol{a}}$ that attempts to predict the difference between estimated log-reflectivities based on a single component (either the real or the imaginary part). In other words, it is trained by minimizing a self-supervised MSE loss $\|g_{\boldsymbol{\theta}}\left(\boldsymbol{a}, \widehat{\boldsymbol{r}}(\boldsymbol{a})\right) - \boldsymbol{\delta}_{\boldsymbol{a}}^{\boldsymbol{b}}\|_2^2$.

Once the network $g_{\boldsymbol{\theta}}$ is trained, the inference of an uncertainty map for a given SAR image can be obtained by combining the estimates obtained separately from the real and imaginary parts: $\frac{1}{2} g_{\boldsymbol{\theta}}(\boldsymbol{a}, \widehat{\boldsymbol{r}}(\boldsymbol{a})) + \frac{1}{2} g_{\boldsymbol{\theta}}(\boldsymbol{b}, \widehat{\boldsymbol{r}}(\boldsymbol{b}))$ which is a good estimation of uncertainty as shown in [26] on images computed by synthetic speckle. Note that this uncertainty estimation method is applicable to any despeckling technique that can be applied to half-look SAR images $\boldsymbol{a}^2$ and $\boldsymbol{b}^2$ (most methods can be adapted to a variable number of looks, i.e., to different speckle levels).

B. CFAR change detection by conformal prediction

To detect changes between two dates t_i and t_j, we form 4 detection maps of the form $\boldsymbol{\gamma}_{\boldsymbol{c}}^{\boldsymbol{d}} = \boldsymbol{\delta}_{\boldsymbol{c}}^{\boldsymbol{d}} / F(\widehat{\boldsymbol{\mu}}_{\boldsymbol{c}}, \widehat{\boldsymbol{\mu}}_{\boldsymbol{d}})$ where $\boldsymbol{c} \in \{\boldsymbol{a}_i, \boldsymbol{b}_i\}$ and $\boldsymbol{d} \in \{\boldsymbol{a}_j, \boldsymbol{b}_j\}$, i.e., $\boldsymbol{c}$ is one of the real or imaginary components of the first date and $\boldsymbol{d}$ is a component of the second date, and $F(\cdot, \cdot)$ denotes a compromise fusion operator [27] (discussed in III-B), combining predicted despeckling uncertainties based on the components $\boldsymbol{c}$ and $\boldsymbol{d}$ (see Fig. 2).

Conformal prediction consists of the calibration of an uncertainty heuristic into an uncertainty metric with mathematical guarantees, like a confidence interval. In our case, by calibrating the distribution of normalized differences $\boldsymbol{\gamma}_{\boldsymbol{c}}^{\boldsymbol{d}}$ in the absence of change, i.e., when $\boldsymbol{c} \equiv \boldsymbol{a}_i$ and $\boldsymbol{d} \equiv \boldsymbol{b}_i$ (the two components extracted from the same date t_i), we can later on identify abnormally large deviations coming from real and imaginary components $\boldsymbol{c}$ and $\boldsymbol{d}$ extracted from images captured at different dates t_i and t_j. This approach corresponds to an application of conformal prediction to anomaly detection.

To threshold these change detection maps with controlled false alarm rates, we learn, thanks to a calibration set $\mathcal{D}$, a function $s_{\mathcal{D}}(\alpha)$ mapping a false alarm rate α to a threshold applicable to all pixels of $\boldsymbol{\gamma}_{\boldsymbol{c}}^{\boldsymbol{d}}$. Conformal prediction provides

[1] Image from only the squared real or imaginary part of the complex image.

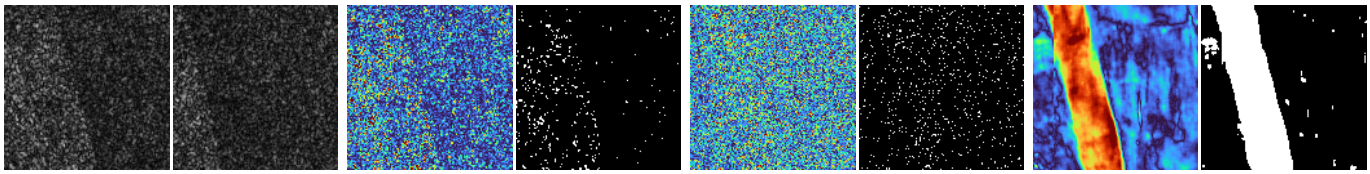

(a) noisy intensities (b) intensity difference (c) log-intensity difference (d) log-reflectivity difference

Fig. 1. Detecting radiometric changes in SAR images can be challenging because of speckle noise: (a) a pair of noisy images (on agricultural area undergoing a change); and changes detected based on (b) intensity difference, (c) log-intensity difference, and (d) log-reflectivity difference.

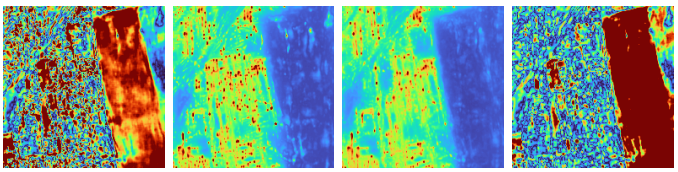

(a) $\boldsymbol{\delta}_{\boldsymbol{c}}^{\boldsymbol{d}}$ (b) $\widehat{\boldsymbol{\mu}}_{\boldsymbol{d}}$ (c) $F(\widehat{\boldsymbol{\mu}}_{\boldsymbol{c}}, \widehat{\boldsymbol{\mu}}_{\boldsymbol{d}})$ (d) $\boldsymbol{\gamma}_{\boldsymbol{c}}^{\boldsymbol{d}}$

Fig. 2. Representation of different steps of the proposed change detection method for $\boldsymbol{c} \equiv \boldsymbol{a}_i$ and $\boldsymbol{d} \equiv \boldsymbol{a}_j$. From left to right, (a) absolute difference of estimated log-reflectivities, (b) estimated uncertainty at t_j, (c) fused estimated uncertainties, and (d) change detection map.

a method to build the function $s_{\mathcal{D}}(\alpha)$ such that the probability that the change detection map exceeds the threshold $s_{\mathcal{D}}(\alpha)$ in the absence of change, at any given pixel p, is close to the prescribed probability α:

$$\alpha - 1/(|\mathcal{D}|+1) \leq \mathbb{P}(\boldsymbol{\gamma}_{\boldsymbol{c}}^{\boldsymbol{d}}(\boldsymbol{p}) > s_{\mathcal{D}}(\alpha)) \leq \alpha\,, \qquad (1)$$

where $|\mathcal{D}|$ is the cardinality of the set $\mathcal{D}$ used to perform the calibration. The function $s_{\mathcal{D}}(\alpha)$ is given by [22]:

$$s_{\mathcal{D}}(\alpha) = \text{Quantile}\left(\mathcal{D}; \lceil (|\mathcal{D}|+1)(1-\alpha)\rceil / (|\mathcal{D}|+1)\right). \qquad (2)$$

The set $\mathcal{D}$ used to perform the calibration is formed by all the pixels of the detection maps $\boldsymbol{\gamma}_{\boldsymbol{c}}^{\boldsymbol{d}}$ computed using pairs $(\boldsymbol{c}, \boldsymbol{d})$ of real and imaginary components extracted from the same date, i.e., for which no change occur other than an independent speckle realization.

Four change detection maps can be produced for each pair of dates (t_i, t_j). After thresholding, these maps can be fused into a single map. We suggest the following fusion of binary change maps:

$$\begin{aligned} \texttt{OR}\Bigg(&\texttt{AND}\left[\boldsymbol{\gamma}_{\boldsymbol{a}_i}^{\boldsymbol{a}_j} > s_{\mathcal{D}}(\alpha); \boldsymbol{\gamma}_{\boldsymbol{b}_i}^{\boldsymbol{b}_j} > s_{\mathcal{D}}(\alpha)\right]\,; \\ &\texttt{AND}\left[\boldsymbol{\gamma}_{\boldsymbol{a}_i}^{\boldsymbol{b}_j} > s_{\mathcal{D}}(\alpha); \boldsymbol{\gamma}_{\boldsymbol{b}_i}^{\boldsymbol{a}_j} > s_{\mathcal{D}}(\alpha)\right]\Bigg). \end{aligned} \qquad (3)$$

This approach offers a good trade-off between limiting false alarms and preserving the probability of detection. Note that, while conformal prediction controls the probability of false alarm of each map, after the fusion this probability is not controlled as precisely: "AND" test on independent maps leads to[2] the approximate false alarm probability α^2, and "OR" leads to[3] the range $[\alpha^2, 2\alpha^2]$ (more precisely $[(\alpha - 1/(|\mathcal{D}|+1))^2, 2\alpha^2]$). Yet, the fusion process is beneficial to the detection of changes because it combines all available information.

[2]Product of the probability of independent random variables

[3]Probability of union of equal to disjoint states

III. Experiments and Analysis

In order to compare the results of our method to the state-of-the-art, we have selected recent unsupervised change detection methods with available code online: Siamese Adaptive Fusion Network (SAFNet) [16] and Feature Fusion of Information Transfer Network (FFITN) [18]. These methods are based on the unsupervised generation of pseudo-labels by fuzzy c-means in order to train, as if it was in a supervised way, a neural network composed of a feature extractor and a classifier.

A. Datasets presentation

First, we use several TerraSAR-X Single Look Complex (SLC) acquisitions in stripmap mode in order to train the despeckling uncertainty estimator. These images have a spatial resolution of 3 meters and a strong speckle noise. The training set consists of two stacks of 26 images of 1024×1024 pixels each, which we later use for change detection, and 24 images of size 4096×4096 to increase the amount of training data. The two 26 images stacks represent Saint-Gervais and Domancy areas in France. Changes between the August 6, 2009, and May 5, 2011, were manually labeled on an area of 384×384 pixels for each stack. We chose these dates because optical images from Google Earth were available on similar dates, which helps with scene understanding and change labeling. The first labeled dataset, represented in the top row of Fig. 3, is an area of Saint-Gervais where the reflectivity of a field changes and a small building is also built. The second is an area of Domancy with very small radiometric changes in some fields, and some complex structural changes without any strong reflectivity differences, in contrast to the buildings in the previous dataset, as shown at the bottom of Fig. 3.

B. Analysis of the change detection method

The Saint-Gervais dataset is used for a study of the proposed method to illustrate the effect of the different parameters both on agricultural and urban areas.

a) Fusion operator F study: First, the choice of the fusion operator F applied to the uncertainties $\widehat{\boldsymbol{\mu}}_{\boldsymbol{c}}$ and $\widehat{\boldsymbol{\mu}}_{\boldsymbol{d}}$ to normalize the estimated reflectivities difference impacts the intensity of changes, in particular when a structure appears or disappears (Fig. 4). When there is a strong evolution of

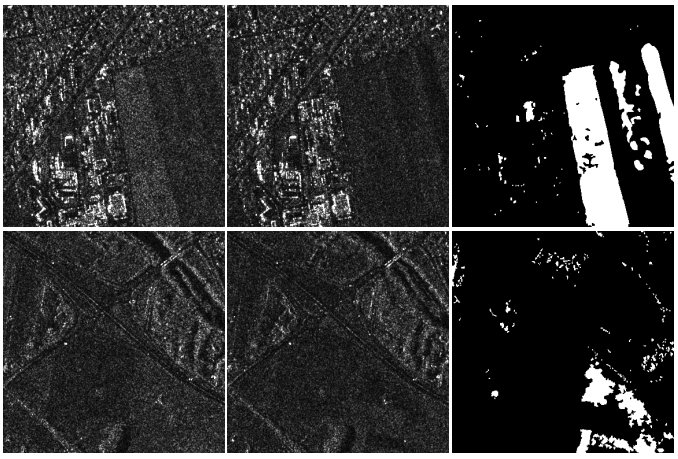

(a) Aug. 6, 2009 (b) May 5, 2011 (c) ground truth

Fig. 3. Saint-Gervais (top row) and Domancy (bottom row) datasets: (a) and (b) represent acquired intensities on Aug. 6, 2009, and May 5, 2011; and (c) is the manually labeled ground truth.

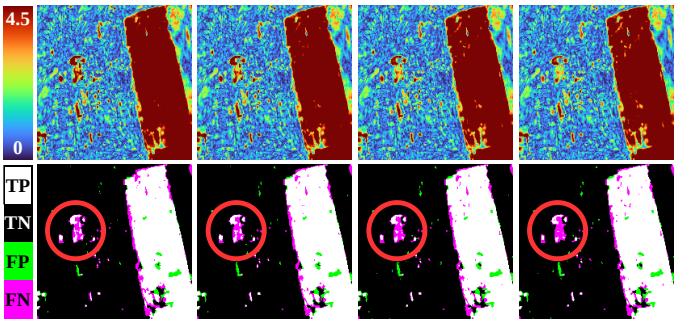

(a) $\frac{2xy}{x+y}$ (b) $\sqrt{xy}$ (c) $\frac{x+y}{2}$ (d) $\sqrt{\frac{x^2+y^2}{2}}$

Fig. 4. Effect of the choice of the fusion operator F on (top row) change detection intensity map, and (bottom row) detected changes after thresholding: (a) harmonic (recommended), (b) geometric, (c) arithmetic, and (d) quadratic mean operator.

the intensity, the uncertainty estimations at the two dates can differ significantly and the choice of F defines how to combine them. The detection maps shown in Fig. 4 for various fusion operators F are quite close (especially harmonic and geometric fusion), we recommend the use of harmonic fusion operator that is the most sensitive to changes.

b) Selection of the false alarm rate α: Low false alarm rates can be selected while correctly detecting changes: α around 10^{-3} is a good compromise, as shown in Fig. 5.

C. Experiments

Based on our previous analysis, we chose a false alarm rate $\alpha = 1/1000$ for calibration by conformal prediction, a harmonic mean operator F to detect more easily the appearance or disappearance of a building, and the logical "OR" test to combine the independent AND-fused change sub-maps. This leads to a false alarm rate between α^2 and $2\alpha^2$ as described in methodology part II-B. We compare here our method to FFITN and SAFNet according to four metrics: (i) the False Alarm Rate (FAR) characterizes the rate of false positive for

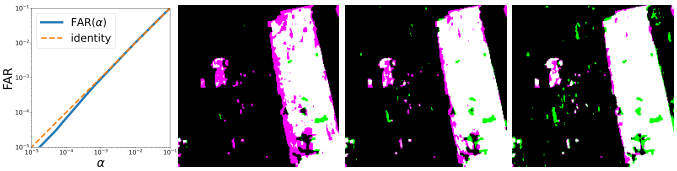

(a) FP fct. α (b) $\alpha = 10^{-4}$ (c) $\alpha = 10^{-3}$ (d) $\alpha = 10^{-2}$

Fig. 5. Effect of false alarm rate choice on change detection. (a) is a plot of the mean false alarm rate for each date in Saint-Gervais stack, after calibration by Domancy 26 images stack, as a function of α. (b), (c), and (d) show changes detected in Saint-Gervais between dates of interest, with the same color code as in Fig. 4.

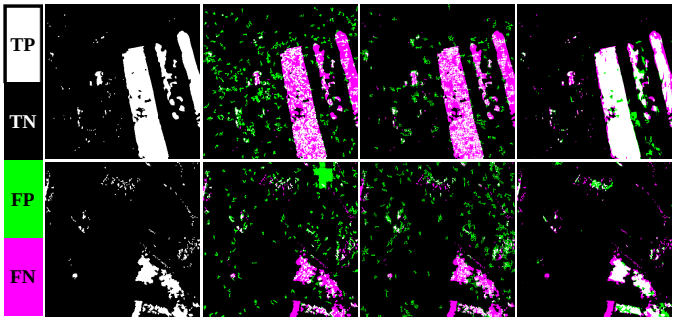

(a) ground truth (b) FFITN (c) SAFNet (d) **proposed**

Fig. 6. Results on (top row) Saint-Gervais and (bottom row) Domancy datasets. From left to right, (a) ground truth and change detection by (b) FFITN, (c) SAFNet, and (d) **proposed**.

every pixel labeled as unchanged; (ii) the Overall Error (OE) is the number of errors over the number of pixels; (iii) the Precision (Pre) is the rate of true positive over the number of predicted true label; (iv) finally, the F1-score (F1) is useful for unbalanced classification problems because it characterizes the number of true positive as a function of the overall error. With TP, TN, FP and FN denoting the true positive, true negative, false positive and false negative, respectively, we have:

$$\text{FAR} = \text{FP}/(\text{TN} + \text{FP}) \tag{4}$$

$$\text{OE} = (\text{FP} + \text{FN})/(\text{TP} + \text{TN} + \text{FP} + \text{FN}) \tag{5}$$

$$\text{Pre} = \text{TP}/(\text{TP} + \text{FP}) \tag{6}$$

$$\text{F1} = 2\text{Pre} \cdot \text{Rec}/(\text{Pre} + \text{Rec}) \tag{7}$$

with $\text{Rec} = \text{TP}/(\text{TP} + \text{FN})$.

On both Domancy and Saint-Gervais datasets Fig. 6, we can see that the false alarm rate is lower with our method than with selected methods, but is higher than the desired false alarm rate ($\sim 1/1.000.000$): this can be explained by the imprecision of the manually labeled change maps since it is reasonable to assume that they contain more than 5% errors. Our method performs better on hard to detect changes. A change such as the appearance of a building, which is characterized by a high intensity difference and a new spatial structure, is more easily detected by FFITN and SAFNet because they take spatial correlation into account. However, we should note that FFITN training is stopped when the κ-score with the ground truth is the best, so this method can not be considered as fully unsupervised. For more subtle changes, such as an evolution

TABLE I
CUMULATED EVALUATION ON SAINT-GERVAIS AND DOMANCY DATASETS

Methods	**FAR↓ (%)**	**OE↓ (%)**	**Pre↑ (%)**	**F1↑ (%)**
FFITN/-desp.	5.95 / 3.87	12.4 / 6.53	47.6 / 72.0	43.5 / 72.9
SAFNet/-desp.	4.34 / 5.25	11.1 / 7.81	54.8 / 65.3	45.6 / 69.0
Proposed	**1.66**	**4.27**	**86.1**	**81.0**

"-desp." means that the method is applied to estimated reflectivities.

of the reflectivity in a field, our method outperforms the others because it is more robust to speckle noise. We should also note that applying FFITN and SAFNet on despeckled reflectivities improves performances as shown in Table I.

Finally, we can show that the computational cost of our method is much lower than for the other two methods. To do this, we must divide the duration into three parts: preprocessing, which does not apply to FFITN and SAFNet, training and inference. The case of our method is a bit particular because, unlike other methods, the training (of the uncertainty estimation network and calibration step) does not need to be updated for new image stacks. Moreover, the inference consists in the application of the determined threshold during training to the preprocessed image, i.e. the rate of the absolute value of the log-reflectivity difference divided by fused uncertainty estimations, both of which have to be estimated. On the same laptop with a NVIDIA RTX™ 2000 Ada GPU, training and inference of FFITN and SAFNet take about 14 and 4 minutes for a couple of 384×384 pixels images, respectively, while the steps of our method take half a second (3.2 seconds for 1024×1024 images).

IV. CONCLUSION

In this paper, we proposed an unsupervised radiometric change detection method for SLC SAR images. To cope with strong speckle noise, a despeckling method is used. Then, in order to compensate for the non-stationary residual variance, we introduced a normalization by the predicted uncertainties. The decomposition of SAR images into real and imaginary components offers a way to calibrate the change detection method in the absence of change by comparing the reflectivities estimated from the real and imaginary parts of the same observation. We used conformal prediction to control the false alarms in this setting. A data fusion strategy is then applied to exploit all the information available. Our experiments indicate that our method effectively controls the false alarms and presents an improved sensitivity to small radiometric changes compared to techniques from the state-of-the-art.

REFERENCES

[1] W. Shi, M. Zhang, R. Zhang, S. Chen, and Z. Zhan, "Change Detection Based on Artificial Intelligence: State-of-the-Art and Challenges," *Remote Sensing*, Jan. 2020.

[2] Q. Liu, K. Ren, X. Meng, and F. Shao, "Domain Adaptive Cross-Reconstruction for Change Detection of Heterogeneous Remote Sensing Images via a Feedback Guidance Mechanism," *IEEE Trans. Geosci. Remote Sens.*, 2023.

[3] R. Caye Daudt, B. Le Saux, and A. Boulch, "Fully Convolutional Siamese Networks for Change Detection," in *ICIP 2018*, Oct. 2018.

[4] H. Chen, Z. Qi, and Z. Shi, "Remote Sensing Image Change Detection With Transformers," *IEEE Trans. Geosci. Remote Sens.*, 2022.

[5] X. Zhang, S. Cheng, L. Wang, and H. Li, "Asymmetric Cross-Attention Hierarchical Network Based on CNN and Transformer for Bitemporal Remote Sensing Images Change Detection," *IEEE Trans. Geosci. Remote Sens.*, 2023.

[6] M. Zhang, Z. Liu, J. Feng, L. Liu, and L. Jiao, "Remote Sensing Image Change Detection Based on Deep Multi-Scale Multi-Attention Siamese Transformer Network," *Remote Sensing*, Jan. 2023.

[7] Y. Zhang, Y. Zhao, Y. Dong, and B. Du, "Self-Supervised Pretraining via Multimodality Images With Transformer for Change Detection," *IEEE Trans. Geosci. Remote Sens.*, 2023.

[8] T. Zhan, M. Gong, X. Jiang, and E. Zhang, "S3Net: Superpixel-Guided Self-Supervised Learning Network for Multitemporal Image Change Detection," *IEEE Geosci. Remote. Sens. Lett.*, 2023.

[9] Y. Chen and L. Bruzzone, "Self-Supervised Change Detection in Multiview Remote Sensing Images," *IEEE Trans. Geosci. Remote Sens.*, 2022.

[10] T. Celik, "Unsupervised Change Detection in Satellite Images Using Principal Component Analysis and k-Means Clustering," *IEEE Geosci. Remote. Sens. Lett.*, Oct. 2009.

[11] L. Bruzzone and D. Prieto, "Automatic analysis of the difference image for unsupervised change detection," *IEEE Trans. Geosci. Remote Sens.*, May 2000.

[12] M. Gong, L. Su, M. Jia, and W. Chen, "Fuzzy Clustering With a Modified MRF Energy Function for Change Detection in Synthetic Aperture Radar Images," *IEEE Trans. Fuzzy Syst.*, Feb. 2014.

[13] P. L. Rosin and J. Hervás, "Remote sensing image thresholding methods for determining landslide activity," *Int. J. Remote Sens.*, Mar. 2005.

[14] D. Meng, F. Gao, J. Dong, Q. Du, and H.-C. Li, "Synthetic Aperture Radar Image Change Detection via Layer Attention-Based Noise-Tolerant Network," *IEEE Geosci. Remote. Sens. Lett.*, 2022.

[15] H. Zhang, Z. Lin, F. Gao, J. Dong, Q. Du, and H.-C. Li, "Convolution and Attention Mixer for Synthetic Aperture Radar Image Change Detection," *IEEE Geosci. Remote. Sens. Lett.*, 2023.

[16] Y. Gao, F. Gao, J. Dong, Q. Du, and H.-C. Li, "Synthetic Aperture Radar Image Change Detection via Siamese Adaptive Fusion Network," *IEEE J. Sel. Topics Appl. Earth Observ. Remote Sens.*, 2021.

[17] X. Qu, F. Gao, J. Dong, Q. Du, and H.-C. Li, "Change Detection in Synthetic Aperture Radar Images Using a Dual-Domain Network," *IEEE Geosci. Remote. Sens. Lett.*, 2022.

[18] J. Ma, D. Li, X. Tang, Y. Yang, X. Zhang, and L. Jiao, "Unsupervised SAR Image Change Detection Based on Feature Fusion of Information Transfer," *IEEE Geosci. Remote. Sens. Lett.*, 2023.

[19] L. Hu, Q. Liu, J. Liu, and L. Xiao, "PRBCD-Net: Predict-Refining-Involved Bidirectional Contrastive Difference Network for Unsupervised Change Detection," *IEEE Trans. Geosci. Remote Sens.*, 2023.

[20] R. C. Daudt, B. Le Saux, A. Boulch, and Y. Gousseau, "Weakly supervised change detection using guided anisotropic diffusion," *Machine Learning*, June 2023.

[21] A. Mian, G. Ginolhac, J.-P. Ovarlez, and A. M. Atto, "New Robust Statistics for Change Detection in Time Series of Multivariate SAR Images," *IEEE Trans. Signal Process.*, Jan. 2019.

[22] A. N. Angelopoulos and S. Bates, "A Gentle Introduction to Conformal Prediction and Distribution-Free Uncertainty Quantification," Dec. 2022. arXiv:2107.07511 [cs, math, stat].

[23] D. Gudovskiy, S. Ishizaka, and K. Kozuka, "CFLOW-AD: Real-Time Unsupervised Anomaly Detection with Localization via Conditional Normalizing Flows," July 2021. arXiv:2107.12571 [cs].

[24] E. Dalsasso, L. Denis, and F. Tupin, "As If by Magic: Self-Supervised Training of Deep Despeckling Networks With MERLIN," *IEEE Trans. Geosci. Remote Sens.*, 2022.

[25] J. Lehtinen, J. Munkberg, J. Hasselgren, S. Laine, T. Karras, M. Aittala, and T. Aila, "Noise2Noise: Learning Image Restoration without Clean Data," Oct. 2018. arXiv:1803.04189 [cs, stat].

[26] I. Meraoumia, *Deep learning for remote sensing images and their interpretation*. PhD thesis, IPP, Dec. 2023.

[27] I. Bloch, "Information combination operators for data fusion: a comparative review with classification," *IEEE Trans. Syst., Man, Cybern. A, Syst. Humans*, Jan. 1996.